Peculiar magnetotransport properties in epitaxially stabilized orthorhombic Ru^{3+} perovskite LaRuO$_3$ and NdRuO$_3$

Check for updates

Lingfei Zhang[1], **Takahiro C. Fujita** [1]✉, **Yuuki Masutake**[2], **Minoru Kawamura** [3], **Taka-hisa Arima** [3,4], **Hiroshi Kumigashira** [2,5], **Masashi Tokunaga** [3,6] & **Masashi Kawasaki** [1,3]

Complex oxides are interesting materials where multiple physical properties and functionalities can be realized by integrating different elements in a single compound. However, owing to the chemical instability, not all the combinations of elements can be materialized despite the intriguing potential expected from their magnetic and electronic properties. Here we demonstrate an epitaxial stabilization of orthorhombic Ru^{3+} perovskite oxides: LaRuO$_3$ and NdRuO$_3$, and their magnetotransport properties that reflect the difference between non-magnetic La^{3+} and magnetic Nd^{3+}. Above all, an unconventional anomalous Hall effect accompanied by an inflection point in magnetoresistance is observed around 1.3 T below 1 K for NdRuO$_3$, which we propose is possibly related to a non-coplanar spin texture on Nd^{3+} sublattice. These studies not only serve as a new testbed for the interplay between spin-orbit coupling and Coulomb interaction but also open a new avenue to explore topological emergent phenomena in well-studied perovskite oxides.

The interplay between spin-orbit coupling (SOC) and Coulomb correlation has become a central topic in condensed-matter physics[1–3]. This crucial importance has been widely known, especially in 4d and 5d transition metal oxides, where SOC acts on an energy scale comparable to the other energy scales such as bandwidth, crystal field, and Coulomb interaction, etc. This class of materials has attracted considerable attention since the discovery of Mott insulating state in Sr$_2$IrO$_4$[4]. The study has expanded to other heavy transition metal oxides, especially with the d^5 configuration under octahedral crystal field[1,2,5]. In such materials of interest, partially filled 4d or 5d t_{2g}-band are split into an effective $j = 1/2$ doublet and effective $j = 3/2$ quartets as shown in Fig. 1a. Indeed, a number of novel topological phenomena related to the effective $j = 1/2$ states have been reported not only in oxides with Ir^{4+} [5–8] but also in α-RuCl$_3$ with Ru^{3+} as a possible candidate of Kitaev quantum spin liquid[9–11]. Here, we pose a question whether it is possible to stabilize Ru^{3+} state in oxide thin films as in the case of well-studied Ir^{4+}, providing more "knobs" to tune the physical properties by utilizing epitaxial strain or heterointerface.

From the chemistry point of view, the stable oxidation state of Ru is generally +4 or higher in oxides[12]. LnRuO$_3$ (Ln: lanthanide) perovskite oxides (orthorhombic $Pbnm$ phase, as shown in Fig. 1b) are rare exceptions of an oxidation state of Ru^{3+}. Because of difficulties in synthesis, however, studies on LnRuO$_3$ are quite limited; with bulk polycrystals[13–16] and single crystals[17], and their electronic and magnetic properties have not been revealed well, in contrast to AeRu^{4+}O$_3$ (Ae: alkaline earth)[18–21]. Different from AeRu^{4+}O$_3$, LnRuO$_3$ can accommodate magnetic Ln^{3+}, which renders this system an intriguing playground for the magnetic interaction between Ru-4d itinerant electrons and Ln-4f localized moments (Fig. 1c). In this point of view, LnRuO$_3$ is a unique system among Ln-M-O (M: transition metal) complex oxides that can support magnetization from Ln-site and metallic conduction on M-O network at the same time, which is critical for evaluating the magnetic interaction by magnetotransport properties. To address this issue, we summarize electrical conductivity of two well-studied structures: perovskite (LnMO$_3$) and pyrochlore (Ln_2M_2O$_7$) in Fig. 1d, where metallic ones are limited to LaNiO$_3$, LaCuO$_3$, LRO, Pr$_2$Ir$_2$O$_7$, and Ln_2Mo$_2$O$_7$ (Ln = Nd, Sm, Gd)[13,22–25].

Among magnetotransport properties, the Hall effect in magnets has been of great interest, especially after the discovery of topological Hall effect

[1]Department of Applied Physics and Quantum Phase Electronics Center (QPEC), The University of Tokyo, Hongo 7-3-1, Bunkyo-ku, Tokyo 113-8656, Japan. [2]Institute of Multidisciplinary Research for Advanced Materials (IMRAM), Tohoku University, Katahira 2-1-1, Sendai, Miyagi 980-8577, Japan. [3]RIKEN Center for Emergent Matter Science (CEMS), Hirosawa 2-1, Wako, Saitama 351-0198, Japan. [4]Department of Advanced Materials Science, The University of Tokyo, Kashiwanoha 5-1-5, Kashiwa, Chiba 277-8561, Japan. [5]Photon Factory, Institute of Materials Structure Science, High Energy Accelerator Research Organization (KEK), Oho 1-1, Tsukuba, Ibaraki 305-0801, Japan. [6]The Institute for Solid State Physics, The University of Tokyo, Kashiwanoha 5-1-5, Kashiwa, Chiba 277-8581, Japan. ✉e-mail: fujita@ap.t.u-tokyo.ac.jp
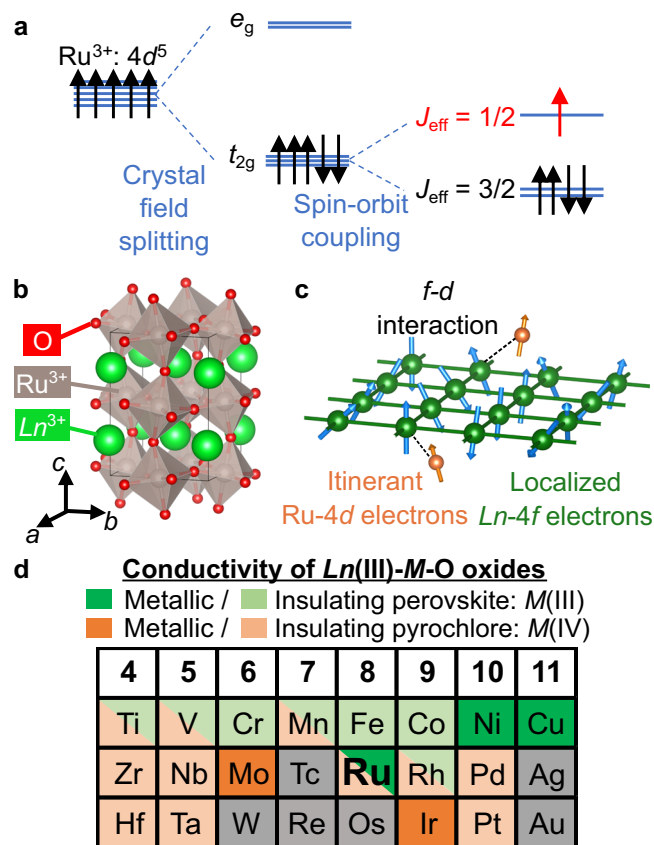
Fig. 1 | Concept of this study. a Band splitting and $4d^5$ electron configuration of Ru^{3+} ion. **b** Schematic of orthorhombic *Pbnm* perovskite structure illustrated by VESTA[43]. **c** Schematic of the interaction between itinerant Ru-4d and localized *Ln*-4f moments with a non-coplanar ordering. **d** Summary of the electrical ground states of *Ln*(III)-*M*-O (*M*: transition metal) perovskite and pyrochlore oxides that have been reported[13,22–25,44–50]. The gray color indicates that there are no reports related to the elements.

(THE). In contrast to the conventional anomalous Hall effect (AHE) in magnets, which appears to be proportional to uniform magnetization *M*, THE originates from topological magnetic states such as magnetic vortex, skyrmion, and non-coplanar spin arrangement. Among various materials, perovskite oxide thin films and heterostructures have been serving as a fertile playground for investigating THE. However, an anomaly seen in magnetic field dependence of AHE deviating from that of *M* cannot always be assigned to THE originating from topological spin texture because the superposition of multiple contributions to conventional AHE can mimic THE signal, which often cannot be ignored in thin films due to the existence of surface/interface, strain, and inhomogeneities[26,27].

In this work, we report the fabrication of the epitaxial thin films of LRO and NdRuO₃ (NRO) with utilizing solid phase epitaxy technique. X-ray absorption spectroscopic (XAS) studies support Ru^{3+} oxidation state in the films. We carry out systematic electrical transport studies in magnetic fields up to 54 T and at temperatures down to 50 mK to investigate the veiled magnetotransport properties of LRO and NRO. We find that both LRO and NRO are metallic though NRO shows a slight upturn below 20 K. LRO exhibits only an ordinary Hall effect, while NRO exhibits a clear signature of AHE, which is successfully deconvoluted from ordinary one with the aid of the high-filed measurements up to 54 T. Especially below 1 K, an unconventional AHE emerges at around 1.3 T concomitantly with an anomaly in magnetoresistance. We propose a possible mechanism of this unconventional AHE in the context of THE related to a non-coplanar spin texture realized in the orthorhombic perovskite structure, while unambiguous assignment requires further challenging experiments due to its appearance

only at very low temperatures below 1 K. These results altogether demonstrate that epitaxial stabilization is a potent activator to push new frontiers of the playground for strongly correlated electrons[28–30] with both sizeable SOC and magnetic interaction that will facilitate new fundaments and high-end applications[31,32].

Results and discussion
Structural properties
Epitaxial LRO and NRO thin films were prepared on SrTiO₃ (STO) (001) substrates by pulsed laser deposition (PLD) and subsequent annealing process (See Methods, Supplementary Note 1, and Supplementary Figs. 1, 3 for the details). X-ray diffraction (XRD) 2θ-θ scan profiles of the films are presented in Fig. 2a, b. From the positions of (002) peaks (pseudocubic setting), out-of-plane lattice constants of LRO and NRO are deduced to be 3.96 Å and 3.94 Å, respectively. The full width at half maximum (FWHM) in rocking curves of (002) peaks (Supplementary Figs. 1d, g) is less than 0.1° for both LRO and NRO films, reflecting high orientation and crystallinity. Thicknesses of the LRO and NRO films are around 6 nm and 9 nm, respectively, which are deduced from x-ray reflectivity measurements at lower incident angles (Supplementary Fig. 1b, e). The root-mean-square roughness of the films is as small as sub-nanometer order before the annealing while the surface becomes several times rougher after the annealing, which is deduced from their atomic force microscope images (Supplementary Fig. 2). The epitaxial relationship between the substrate and the thin films is clarified by the reciprocal space mappings (RSM) presented in Fig. 2c (and Supplementary Fig. 5). The peak of LRO exhibits a slight broadening toward smaller Q_x from the peak position of STO. Since the mismatch between bulk LRO (3.94 Å in pseudocubic setting) and STO substrate (3.905 Å) is as large as 1%, this broadening indicates that the thin film near the interface is fully strained while the rest part is partially relaxed. On the other hand, NRO (3.92 Å in pseudocubic setting), which has less mismatch to STO substrate, does not show such a peak broadening and thus is fully strained. The high quality of the films can be confirmed by TEM images presented in Fig. 2d, e as well. Lattice images in an atomic resolution are clearly seen for thin films epitaxially grown on STO substrate. The formation of orthorhombic perovskite structure is also supported by electron beam diffractions (Supplementary Fig. 4).

Oxidation state of Ru
As evidenced by the XRD and TEM measurements, it is apparent that LRO and NRO films are stabilized as perovskite structures. However, as mentioned above, Ru^{3+} is generally unstable in oxides[12]. To further confirm the oxidation state of Ru, XAS measurements are performed for both LRO and NRO films. Figure 2f and its inset respectively show the wide and near-edge XAS for these thin films in comparison with those for Ru metal (Ru^0), SrRuO₃ (Ru^{4+}), and RuO₂ (Ru^{4+}) as references. As shown in the inset of Fig. 2f, Ru K-edge energies of LRO and NRO are located at the lower energy (reduction) side than those of SrRuO₃ and RuO₂, indicating that the oxidation state of Ru in LRO and NRO is less than +4. The oxidation state is semi-quantitatively evaluated by comparing the Ru K-edge energies of the films with those of reference compounds for Ru^{2+} or Ru^{3+}, as shown in Fig. 2g[33,34]. Here, Ru K-edge energy is defined as the energy at which the normalized absorption intensity decreased by half. The Ru K-edge energies of LRO and NRO are represented by red and blue vertical lines, respectively, while the ones of other compounds are plotted by symbols with the reported oxidation states. Ru K-edge energies of LRO and NRO are located among the ones of standard references for Ru^{3+}; $Ru^{3+}Cl_3$, $Ru^{3+}I_3$, and $[Ru^{3+}(NH_3)_5]$ Cl_3. Therefore, we conclude that Ru predominantly exists as +3 oxidation state in both LRO and NRO films.

Comparison of magnetotransport properties between LaRuO₃ and NdRuO₃
Temperature dependence of longitudinal resistivity (ρ_{xx} – *T* curves) for LRO and NRO is presented in Fig. 3a, b. In Fig. 3a, ρ_{xx} is shown in a logarithmic scale to compare with those in previous studies (dashed lines).
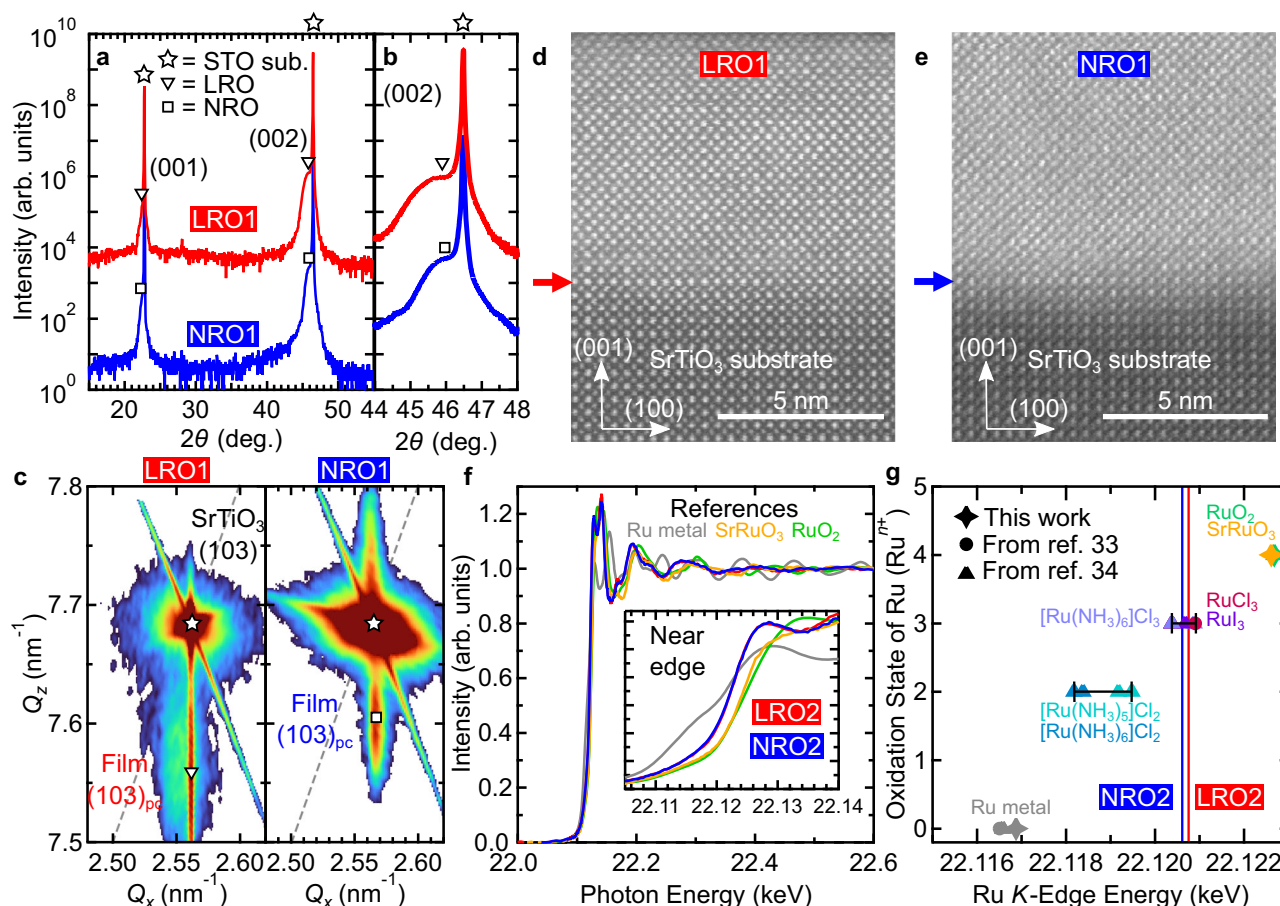
Fig. 2 | Structural properties and valence states of LaRuO₃ and NdRuO₃ thin films. XRD $2\theta\text{-}\theta$ scan profiles (**a**) and magnified data around the (002) peaks (**b**) of LaRuO₃ and NdRuO₃ thin films on SrTiO₃ (001) substrates. Peaks for the substrate, LaRuO₃, and NdRuO₃ are indicated by stars, triangles, and squares, respectively. **c** The XRD reciprocal space mappings around SrTiO₃ (103) peak. The gray broken lines indicate the relaxation lines where a fully relaxed cubic film peak is supposed to be located. TEM image of LaRuO₃ (**d**) and NdRuO₃ (**e**) thin films. The red and blue arrows indicate the position of the interface between the film and substrate. **f** Ru K-edge XAS spectra of LaRuO₃ and NdRuO₃ thin films in comparison with those of Ru⁰ metal, Ru⁴⁺O₂ and SrRu⁴⁺O₃ as references. The intensity was normalized so that the averaged edge jump became unity. The inset shows the enlarged view of near-edge structures. **g** Oxidation state of Ru (Ru^{n+}) versus Ru K-edge energy, which is defined as the energy where the normalized intensity equals 0.5. The vertical red and blue lines correspond to the Ru K-edge energies of the LaRuO₃ and NdRuO₃ thin films, respectively. Symbols of stars, circles, and triangles refer to the data from the present measurement, ref. [33], and SPring-8 BENTEN database[34], respectively.

For LRO, our thin film sample is metallic down to 5 K and ρ_{xx} slightly increases at lower temperatures. Compared with the works by refs. [13,14] for polycrystalline samples, our LRO film has a lower ρ_{xx} by one order of magnitude. For NRO, in striking contrast to the insulating behavior reported in the bulk polycrystalline sample[15], our thin film is metallic down to 20 K and shows a weak upturn in ρ_{xx} with further cooling. This improvement in conductivity, plausibly originating from the high crystallinity and less grain boundary scattering in our epitaxial thin films, endows an opportunity to examine magnetotransport properties of the two contrasting LRO and NRO with non-magnetic La³⁺ and magnetic Nd³⁺, respectively.

Magnetic field (B) dependence of magnetoresistance ratio (MRR (%) $\equiv [\rho_{xx}(B)/\rho_{xx}(0) - 1] \times 100$) and Hall resistivity ($\rho_{yx}$) up to 9 T measured by Physical Properties Measurement System (PPMS, Quantum Design Co.) are presented in Fig. 3c–f. For LRO, MRR increases monotonically (Fig. 3c), and ρ_{yx} is linear (Fig. 3d) to the magnetic field down to 2 K. These behaviors suggest a paramagnetic and metallic state in LRO, which is consistent with previous reports[13,14]. On the other hand, NRO exhibits peculiar behaviors at low temperatures in both MRR (Fig. 3e) and ρ_{yx} (Fig. 3f). Negative MRR, which is a typical response in magnetic materials, is observed below 5 K. Above 30 K, ρ_{yx} is linear but exhibits a sign reversal at around 60 K. Below 30 K, ρ_{yx} is no longer linear to the magnetic

field. What is more, at 0.5 K, a unique bulge in MRR and a hump structure in ρ_{yx} are observed at an identical magnetic field of ~1.3 T (Also discussed later on in relation to the unconventional Hall effect in NdRuO₃). These distinct behaviors observed only in NRO at low temperatures suggest an essential role of an interaction between Nd-4f spins and Ru-4d electrons in magnetotransport properties, compelling us to perform further measurements with a pulsed high magnetic field.

Magnetotransport properties of NdRuO₃ under high magnetic field

Magnetic field dependence of MRR and ρ_{yx} up to 54 T for NRO are presented in Fig. 4a, b, respectively, together with the results measured with a PPMS up to 9 T (thick lines). As presented in Fig. 4a, MRR increases monotonically up to 54 T above 10 K. Below 10 K, MRR decreases at lower fields with a minimum at $B \approx 10$ T and turns to increase at higher fields similar to the ones above 10 K. This can be seen more clearly in Fig. 4d, where $\rho_{xx} - T$ curves under different magnetic fields are shown. Intriguingly, the slopes of ρ_{yx} saturate at a similar negative value at higher fields regardless of the measurement temperatures (Fig. 4b). Because of this, ordinary Hall coefficient (R_H) can be deduced from linear fittings of ρ_{yx} between 45 T and 54 T. As presented in Fig. 4e, R_H has little temperature dependence below 150 K. Therefore, with the help of the high-field
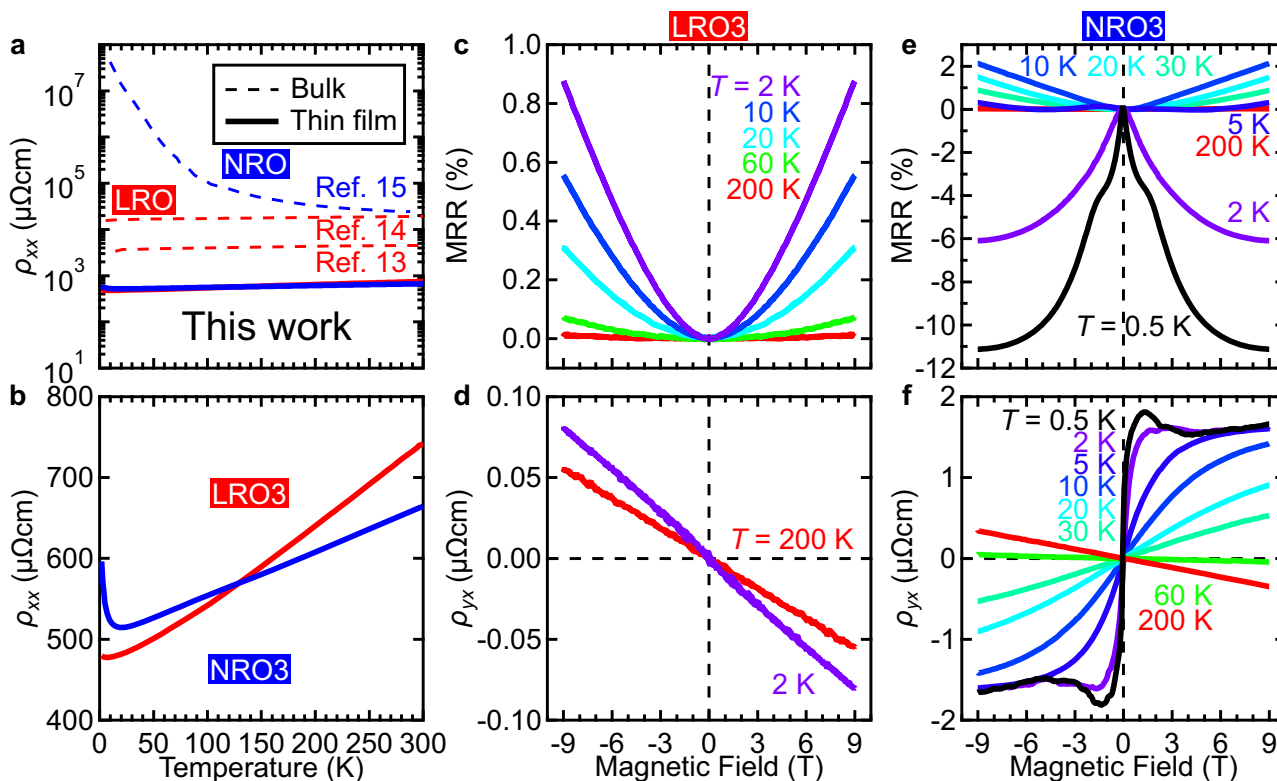
Fig. 3 | Magnetotransport properties of LaRuO₃ and NdRuO₃ thin films.
a, b Temperature dependence of longitudinal resistivity (ρ_{xx}) compared with those in previous reports of polycrystalline bulk samples[13–15]. The data are plotted in logarithmic (**a**) and linear (**b**) scales. Magnetic field dependence of magnetoresistance ratio (MRR) and Hall resistivity (ρ_{yx}) for LaRuO₃ (**c, d**) and NdRuO₃ (**e, f**) at selected temperatures.

measurements, the sign reversal of ρ_{yx} observed in Fig. 3f is revealed to be irrelevant to a carrier-type change.

Anomalous Hall effect of NdRuO₃
Having clarified that the carrier-type of NRO is electron regardless of temperatures, we can discuss the AHE of NRO. With using the deduced R_{H} in Fig. 4e, anomalous Hall resistivity ρ_{AHE} is defined as $\rho_{\mathrm{AHE}}(B) = \rho_{yx}(\mathrm{B}) - R_{\mathrm{H}}B$ and presented in Fig. 4c. AHE is an important electrical transport phenomenon attracting extensive interest in both fundamental physics and potential applications[26,35]. Indeed, NRO unveils various AHE originating from different magnetic interactions depending on temperatures and magnetic fields as we discuss below.

At high temperatures, AHE emerges below ~100 K while ρ_{yx} is linear to the magnetic field above 120 K. Since 100 K is too high for Ln^{3+} ions to be ordered in perovskite oxides[36], AHE in this temperature range is supposed to originate from the magnetism of Ru³⁺ induced by the applied magnetic field. At lower temperatures, AHE at the high-field region shows almost no temperature dependence while it develops much faster at the low field region below 20 K. This feature can be also confirmed clearly in the temperature dependence of ρ_{AHE} at various magnetic fields ($\rho_{\mathrm{AHE}}(B) - T$ curve) shown in Fig. 4f. Here, ρ_{AHE} increases dramatically below 20 K even at 1 T, which is distinct from other curves measured at higher magnetic fields.

Finally, below 1 K, AHE starts to show a distinct behavior. Figure 5a shows ρ_{AHE} below 5 K and 4 T. At 0.8 K and 0.5 K, clear hump structures are observed at ~1.3 T while ρ_{AHE} almost monotonically increases as a function of B above 1.5 K. Furthermore, as presented in Fig. 5b, inflection points are observed for MRR at the same field range below 0.8 K. To compare the relationship between these two anomalies, we show the magnetic field derivatives of ρ_{AHE} and MRR at 0.5 K in Fig. 5c. The hump structure in ρ_{AHE} and the inflection point in MRR appear almost at the same magnetic field, which is indicative of the same origin for these two phenomena: plausibly a magnetic one.

Since AHE is generally proportional to the magnetization M, it is didactic to compare the observed AHE with the magnetic properties measured for another thick NRO film (NRO5) down to 2 K (See Supplementary Note 5 and Supplementary Figs. 8, 9). As presented in Supplementary Fig. 9a, M becomes detectable at ~100 K, which coincides with the emergence of the AHE shown in Fig. 4c. In the range of 30–100 K, M increases linearly to the magnetic field up to 7 T, indicating that NRO is in an AFM or a paramagnetic (PM) phase. Considering that there is no anomaly in the $\rho_{xx} - T$ curve usually concomitant with magnetic transitions, we speculate that NRO may be PM in this temperature range, and magnetic moments of Ru³⁺ induced by the applied magnetic field lead to the AHE. At temperatures lower than 20 K, M becomes non-linear to the magnetic field, which can be the reason for the steep increase in AHE at low fields in Fig. 4c, f. This alludes to the existence of an additional magnetic component that is sensitive to magnetic field only at lower temperatures, which is attributable to Nd³⁺ moments, yet they may not be ordered in the temperature range. We also compare the magnetic field dependence of magnetization ($M - H$ curve) with the $\rho_{\mathrm{AHE}} - H$ curve for this thick NRO film, and find an almost perfect agreement between them above 10 K (Supplementary Fig. 9).

Possible origin of unconventional anomalous Hall effect of NdRuO₃
Finally, we discuss the origin of the hump structure in AHE at lower temperatures than 1 K. As previously reported, such a hump structure could arise from the trivial superposition of multiple contributions to conventional AHE as we mentioned in Introduction, which has been reported in many studies of SrRuO₃ thin films and heterostructures. At present, we cannot exclude the possibility that the hump structure in NdRuO₃ also originates from such contributions from conventional AHE. On the other hand, LnRuO₃ studied here are distinctive materials that can accommodate magnetic Ln^{3+} ions different from SrRuO₃. Therefore, we attempt to propose an alternative mechanism in the framework of THE due to Nd³⁺

Fig. 4 | Magnetotransport properties of NdRuO₃ thin film measured with a pulsed high field magnet. Magnetic field dependences of MRR (**a**), ρ_{yx} (**b**), and anomalous Hall resistivity (ρ_{AHE}, **c**) at various temperatures. See the main text for the definition of ρ_{AHE}. Both of the results measured with a PPMS (thick lines below 9 T) and the pulsed high field magnet (thin lines) are shown. The vertical dotted line indicates the position of $B = 9$ T. The oscillation patterns appeared at 1.4 K are merely from noise because of the low measurement current which is employed to suppress the Joule heating (See Methods for details). **d** Temperature dependence of ρ_{xx} at $B = 0$, 9 (with a PPMS) and 54 T (with the pulsed high field magnet). **e** Temperature dependence of Hall coefficient (R_H) deduced by a linear fitting of ρ_{yx} between 45 and 55 T. An optical image of the device structure for the transport measurements. Ni/Au electrodes (dark areas) are deposited on the film and then it is scribed (white dotted lines indicate the scribed lines) to fabricate a Hall bar structure highlighted by the red colored area. **f** Temperature dependence of ρ_{AHE} at selected magnetic field. The curves for $B = 1$ and 54 T are presented by lines with open and filled circles.
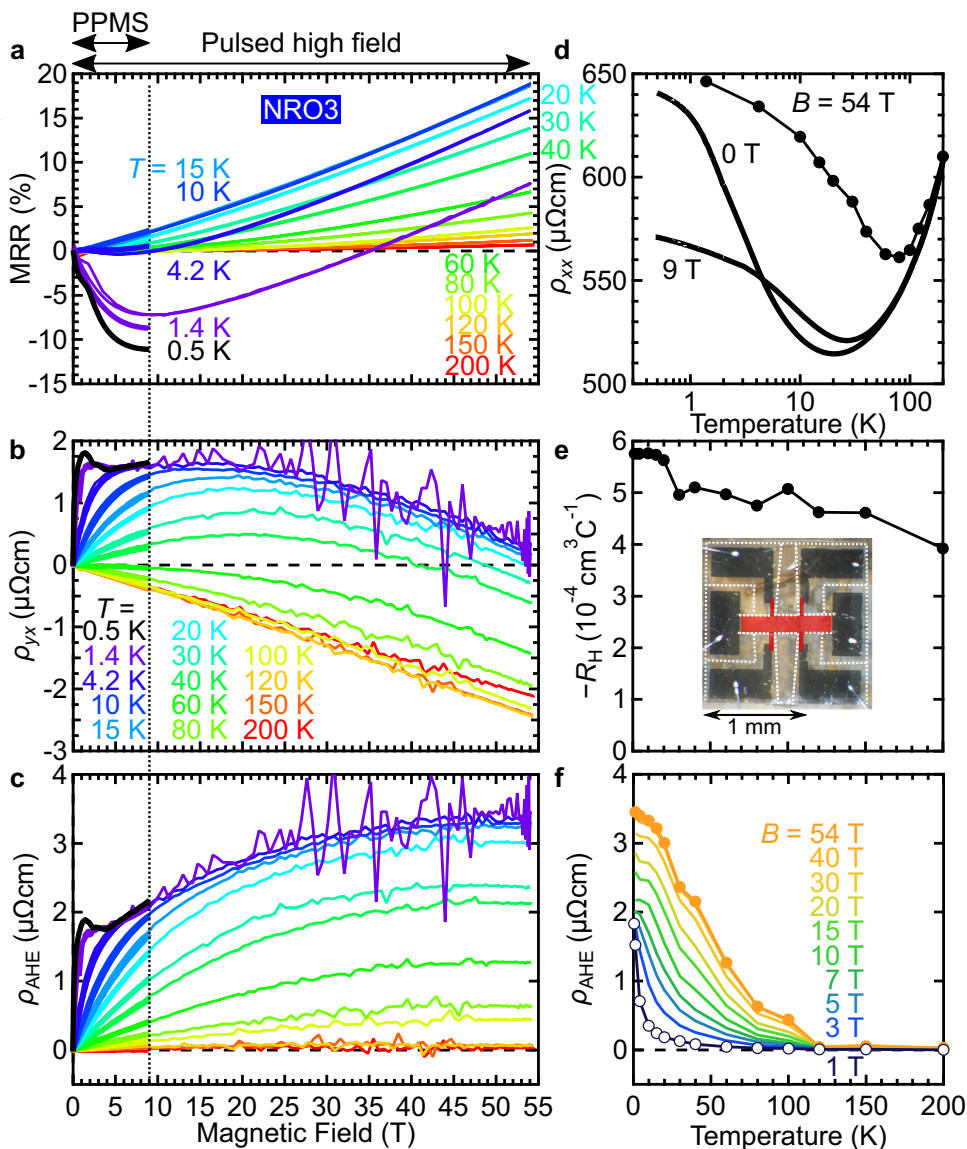
moments. Here, we assume THE characteristic of the "non-coplanar" magnetic structure with finite scalar spin chirality defined as $\chi_S = \mathbf{S}_i \cdot (\mathbf{S}_j \times \mathbf{S}_k)$ (See inset of Fig. 5a)[35]. Actually, non-coplanar spin textures are ubiquitous in M-site of orthorhombic $LnMO_3$ including NdMO_3 (M: 3d transition metal)[36]. For example, in NdMO_3 (M: Cr, Fe, etc.), employing Bertaut's notation[37], a non-coplanar $G_bA_aF_c$ spin texture of M^{3+} moments has been widely confirmed. On the other hand, for Nd^{3+} moments, G_bA_a (M = Sc, In) or C_c (M = Cr, Co, Ga) textures are commonly observed while both are coplanar[36,38–40]. Considering the more itinerant nature of Ru-4d electron, realization of the non-coplanar $G_bA_aF_c$ spin structure of Ru^{3+} moments is unlikely in NRO, thus we speculate that finite χ_S is mediated by the spin texture of Nd^{3+} moments. We are aware that this speculation should be supported by direct observation of magnetic structure or measurements of elemental-sensitive techniques such as neutron diffraction and x-ray magnetic circular dichroism. However, because of the thin film nature of the sample and the low ordering temperature (~1 K), they are not feasible at present. Therefore, we propose a possible mechanism based on the crystal symmetry as discussed below (Also see Supplementary Notes 6 and 7).

As a starting point, we hypothesize that Nd^{3+} moments in NRO have G_bA_a order as the ground state (Supplementary Fig. 10c) and turn into ferromagnetic (FM) order (Supplementary Fig. 10e) at ~2.5 T, where THE disappears (Fig. 5a), since χ_S should vanish in the FM state. This type of

transition is indeed reported in GdFeO₃, where Gd^{3+} moments take G_bA_a ground state and turn into FM state at about 5 T and 2 K[41]. As mentioned above, the spin structure of G_bA_a order is coplanar, where Nd^{3+} moments are confined within the ab-plane of orthorhombic setting. In our NRO film, the ab-plane is perpendicular to the film surface, which is confirmed by electron beam diffraction and RSM (See Supplementary Note 3 and Supplementary Table 3). Thus, when a magnetic field is applied perpendicular to the film surface, it is parallel to the ab-plane. With increasing the magnetic field, Nd^{3+} moments are aligned toward the field direction, leading to an induced FM order. We suggest, during this transition, Nd^{3+} moments point toward the c-axis and form a non-coplanar spin texture as presented in Fig. 5d (Also see Supplementary Fig. 10d) instead of simply rotating in the ab-plane, which we conjecture can be a source of finite χ_S. Here in NRO, because of the square lattice, the definition of χ_S is not as straightforward as in the case of well-known triangular lattices. Yet, by summing up χ_S from all the possible combinations of the three spins, it can be achieved. Although a more detailed discussion is provided in Supplementary Note 7, χ_S from each contribution is indeed canceled out when the crystal structure has a high symmetry (See Supplementary Table 4, and Supplementary Figs. 11, 12). We thus speculate that there must be some causes for breaking the bulk crystal symmetry, which will be clarified by further studies for direct evidence.
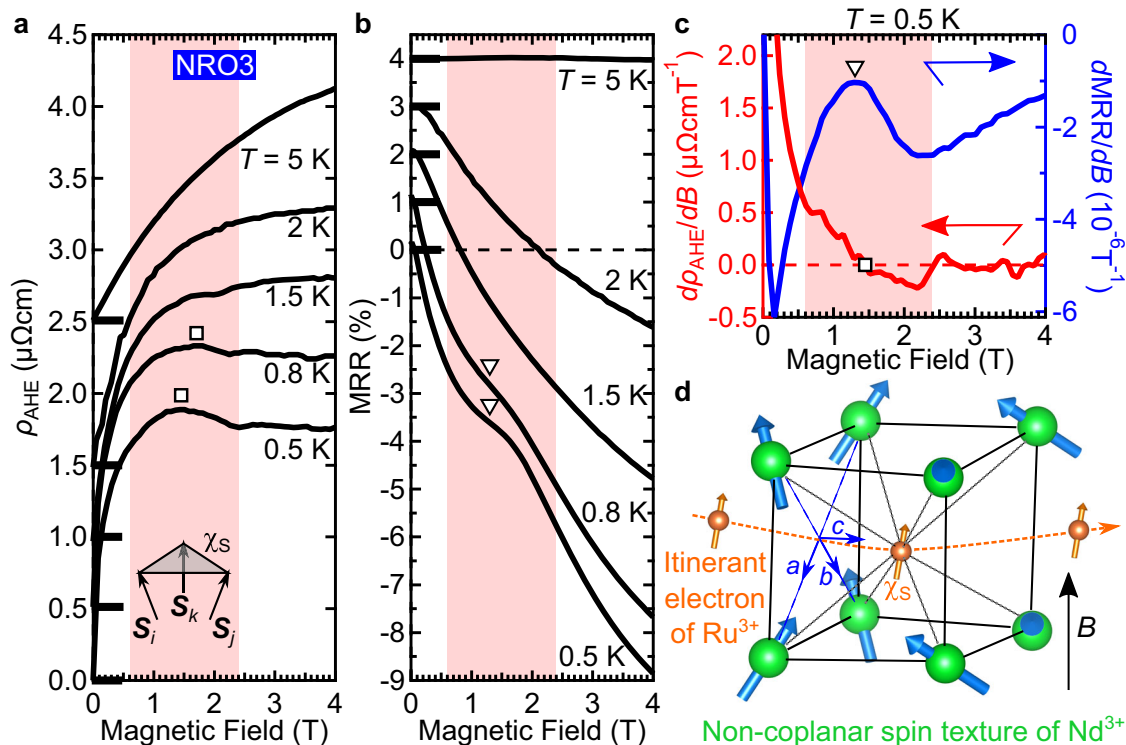
Fig. 5 | Unconventional Hall effect in NdRuO₃ thin film. Magnetic field dependence of ρ_{AHE} (**a**) and MRR (**b**) in the NRO film below 5 K at low-field region ($B \leq 4$ T) with vertical offsets for clarity. The results of 0.5, 2, and 5 K are identical to the ones presented in Fig. 3e, f. For each curve in (**a, b**), its origin at $B = 0$ is indicated by a thick horizontal bar. Inset of (**a**) is a schematic of a non-coplanar spin texture that produces scalar spin chirality χ_S. The peak position of AHE and inflection point of MRR are indicated by square and triangle, respectively. **c** Magnetic field dependence of magnetic field derivatives of ρ_{AHE} (red curve, left axis) and MRR (blue curve, right axis) at 0.5 K. The square and triangle in (**c**) indicate the zero point in $d\rho_{AHE}/dB$ (i.e., peak in ρ_{AHE}) and the peak in $dMRR/dB$ (i.e., an inflection point in MRR) around 1.3 T, respectively. The red-colored areas in (**a–c**) highlight the field region where the anomalies are observed at 0.5 K. **d** Schematic of a possible mechanism to generate the topological Hall effect. Itinerant electrons of Ru³⁺ interact with localized Nd³⁺ moments and acquire χ_S induced by non-coplanar spin texture of Nd³⁺. Note that Ru³⁺ locates at the body center of the deformed cube formed by Nd³⁺.

Conclusion

In conclusion, we have successfully stabilized perovskite LRO and NRO with Ru³⁺ in the epitaxial thin film form as a new materials platform to investigate the interaction between Ru−4d and Ln-4f electrons. Magnetotransport measurements highlight the clear difference between LRO and NRO reflecting the absence/presence of magnetic moments on Ln-site as we designed. Especially, only NRO exhibits an anomalous Hall effect, wherein interaction among Ru³⁺ moments below 100 K, and between Nd³⁺ and Ru³⁺ moments below 20 K play important roles. Above all, we capture an unconventional AHE below 1 K. We propose a possible mechanism to realize the unconventional AHE in the framework of topological spin texture based on the common spin configuration of orthorhombic perovskite NdMO_3.

Methods
Sample Preparation

Epitaxial LRO and NRO thin films were prepared on STO (001) substrates by pulsed laser deposition (PLD) and subsequent annealing process. This procedure is the so-called solid phase epitaxy, where the precursor seed layer is epitaxially crystallized by annealing[42]. Targets for LRO and NRO were prepared by solid-phase reaction using Ln_2O_3 ($Ln =$ La or Nd) and RuO₂ powders as starting materials. To avoid the deficiency of Ru, Ln_2O_3 and RuO₂ were mixed by the molar ratio of Ln:Ru = 1:1.25. The mixed powders were milled and calcined for 24 h at 1,150 °C in air. Powder X-ray diffraction (XRD) confirmed that La₃.₅Ru₄O₁₃ and Nd₂Ru₂O₇ were respectively formed in LRO and NRO targets. The excess Ru remained as RuO₂ in both targets. Before deposition, STO substrates were annealed in-situ at 950 °C under 10^{-5} Torr oxygen to obtain a clear step-terrace structure with single-unit-cell height. The films were deposited at a substrate temperature of

600 °C and an oxygen pressure of 10^{-4} Torr after the optimization of growth conditions (See Supplementary Fig. 1a). KrF excimer laser ($\lambda = 248$ nm) pulses with a frequency of 5 Hz and a fluence of ∼2 J cm⁻² were employed to ablate the targets. After deposition, the as-grown thin films were annealed with RuO₂ powder in a tube furnace at 1000 °C for 2 h under 160 ml min⁻¹ N₂ flow (Supplementary Fig. 3). RuO₂ powder works as a supplying source for compensating Ru into the as-grown thin films to form the perovskite structure.

Structural characterization

The structural properties of the samples were characterized by XRD (Smart Lab, Rigaku) and transmission electron microscope (TEM) at room temperature. The oxidation state of Ru in the films was analyzed by X-ray absorption spectroscopy (XAS) measurements around the Ru K-edge. The XAS measurements were conducted in the fluorescence mode at BL14B2 beamline, SPring-8.

Magnetotransport measurements

For the magnetotransport measurements, a Hall bar structure was fabricated by a scriber, and Ni (10 nm) and Au (50 nm) electrodes were deposited by electron beam evaporation. Aluminum wires were attached to the six electrodes to obtain longitudinal (ρ_{xx}) and Hall (ρ_{yx}) resistivities by four-terminal measurements. A typical device structure is presented in the inset of Fig. 4e. The magnetic field was applied perpendicularly to the film surface; ρ_{xx} and ρ_{yx} were deduced by conventional symmetrization and anti-symmetrization procedures, respectively. Magnetotransport measurements were performed with a 9 T superconducting magnet equipped with a liquid He cryostat (PPMS, Quantum Design Co.) down to 0.5 K. Above 2 K, the measurement current I_m was set to 50 μA. Below 2 K, I_m was reduced to

3 µA to prevent the Joule heating. Additional transport properties at lower temperatures and higher magnetic fields were measured with a dilution refrigerator down to 50 mK (See Supplementary Note 4 and Supplementary Figs. 6, 7) and a pulsed magnet up to 54 T, respectively. For the high field measurements, I_m was set to 400 µA above 4.2 K and 60 µA at 1.4 K to suppress the Joule heating. For the dilution refrigerator measurements, to minimize the Joule heating, I_m was set to 0.1 µA.

Magnetic measurements
Magnetization measurements for NRO were performed with a superconducting quantum interference device magnetometer (MPMS3, Quantum Design Co.) down to 2 K and up to 7 T. Since it was challenging to detect the magnetic moment signal in an ultra-thin film, a 37-nm-thick NRO film was prepared for the magnetic measurements. A bare SrTiO₃ substrate was also measured to subtract the diamagnetic contribution originating from the substrate. The summary of magnetic properties is presented in Supplementary Note 5, and Supplementary Figs. 8, 9.

Summary of samples
Several LRO and NRO films were employed for the various measurements mentioned above. See Supplementary Note 2 and Supplementary Tables 1, 2 for the summary of these samples.

Data availability
All data are available in the main text or the supplementary materials.

References
1. Witczak-Krempa, W., Chen, G., Kim, Y. B. & Balents, L. Correlated quantum phenomena in the strong spin-orbit regime. *Annu. Rev. Condens. Matter Phys.* **5**, 57–82 (2014).
2. Rau, J. G., Lee, E. K. H. & Kee, H. Y. Spin-orbit physics giving rise to novel phases in correlated systems: iridates and related materials. *Annu. Rev. Condens. Matter Phys.* **7**, 195–221 (2016).
3. Maryenko, D. et al. Interplay of spin–orbit coupling and Coulomb interaction in ZnO-based electron system. *Nat. Commun.* **12**, 3180 (2021).
4. Kim, B. J. et al. Novel J_{eff} = 1/2 Mott state induced by relativistic spin-orbit coupling in Sr₂IrO₄. *Phys. Rev. Lett.* **101**, 076402 (2008).
5. Bertinshaw, J., Kim, Y. K., Khaliullin, G. & Kim, B. J. Square lattice iridates. *Annu. Rev. Condens. Matter Phys.* **10**, 315–336 (2019).
6. Yamada, R. et al. Field-induced multiple metal-insulator crossovers of correlated Dirac electrons of perovskite CaIrO₃. *npj Quantum Mater.* **7**, 13 (2022).
7. Kitagawa, K. et al. A spin-orbital-entangled quantum liquid on a honeycomb lattice. *Nature* **554**, 341–345 (2018).
8. Takagi, H., Takayama, T., Jackeli, G., Khaliullin, G. & Nagler, S. E. Concept and realization of Kitaev quantum spin liquids. *Nat. Rev. Phys.* **1**, 264–280 (2019).
9. Banerjee, A. et al. Neutron scattering in the proximate quantum spin liquid α-RuCl₃. *Science* **356**, 1055–1059 (2017).
10. Kasahara, Y. et al. Majorana quantization and half-integer thermal quantum Hall effect in a Kitaev spin liquid. *Nature* **559**, 227–231 (2018).
11. Yokoi, T. et al. Half-integer quantized anomalous thermal Hall effect in the Kitaev material candidate α-RuCl₃. *Science* **373**, 568–572 (2021).
12. Greenwood, N. N. & Earnshaw, A. *Chemistry of the elements*. (Butterworth-Heinemann, 1997).
13. Bouchard, R. J. & Weiher, J. F. LaₓSr₁₋ₓRuO₃: a new perovskite series. *J. Solid State Chem.* **4**, 80–86 (1972).
14. Sugiyama, T. & Tsuda, N. Electrical and magnetic properties of Ca₁₋ₓLaₓRuO₃. *J. Phys. Soc. Japan* **68**, 3980–3987 (1999).
15. Sinclair, A. et al. Synthesis and properties of lanthanide ruthenium(III) oxide perovskites. *Angew. Chem. Int. Ed.* **53**, 8343–8347 (2014).
16. Ji, K. et al. YRuO₃: a quantum weak ferromagnet. *Phys. Rev. Mater.* **4**, 091402 (2020).
17. Patel, B. K., Kolambage, M. T. K., McMillen, C. D. & Kolis, J. W. Hydrothermal synthesis of lanthanide ruthenate single crystals. *J. Cryst. Growth* **602**, 126979 (2022).
18. Koster, G. et al. Structure, physical properties, and applications of SrRuO₃ thin films. *Rev. Mod. Phys.* **84**, 253–298 (2012).
19. Cheng, J. G. et al. High-pressure synthesis of the BaIrO₃ perovskite: A Pauli paramagnetic metal with a Fermi liquid ground state. *Phys. Rev. B* **88**, 205114 (2013).
20. Matsuno, J. et al. Interface-driven topological Hall effect in SrRuO₃-SrIrO₃ bilayer. *Sci. Adv.* **2**, e1600304 (2016).
21. Takiguchi, K. et al. Emergence of Weyl fermions in an epitaxial ferromagnetic oxide. *Nat. Commun.* **11**, 4969 (2020).
22. Torrance, J. B., Lacorre, P., Nazzal, A. I., Ansaldo, E. J. & Niedermayer, C. Systematic study of insulator-metal transitions in perovskites RNiO₃ (R = Pr, Nd, Sm, Eu) due to closing of charge-transfer gap. *Phys. Rev. B* **45**, 8209–8212 (1992).
23. Arima, T., Tokura, Y. & Torrance, J. B. Variation of optical gaps in perovskite-type 3d transition-metal oxides. *Phys. Rev. B* **48**, 17006–17009 (1993).
24. Matsuhira, K., Wakeshima, M., Hinatsu, Y. & Takagi, S. Metal-insulator transitions in pyrochlore oxides $Ln_2Ir_2O_7$. *J. Phys. Soc. Japan* **80**, 094701 (2011).
25. Greedan, J. E., Sato, M., Ali, N. & Datars, W. R. Electrical resistivity of pyrochlore compounds $R_2Mo_2O_7$ (R = Nd, Sm, Gd, Tb, Y). *J. Solid State Chem.* **68**, 300–306 (1987).
26. Wang, H., Dai, Y., Chow, G.-M. & Chen, J. Topological Hall transport: Materials, mechanisms and potential applications. *Prog. Mater. Sci.* **130**, 100971 (2022).
27. Kimbell, G., Kim, C., Wu, W., Cuoco, M. & Robinson, J. W. A. Challenges in identifying chiral spin textures via the topological Hall effect. *Commun. Mater.* **3**, 19 (2022).
28. Fujita, T. C., Zhang, L. F. & Kawasaki, M. Antiferromagnetic metallic state as proved by magnetotransport in epitaxially stabilized perovskite PbRuO₃. *Phys. Rev. Mater.* **4**, 031401 (2020).
29. Maruyama, T., Chikamatsu, A., Onozuka, T. & Hasegawa, T. Magnetotransport properties of perovskite EuNbO₃ single-crystalline thin films. *Appl. Phys. Lett.* **113**, 032401 (2018).
30. Kozuka, Y. et al. Epitaxially stabilized EuMoO₃: a new itinerant ferromagnet. *Chem. Mater.* **24**, 3746–3750 (2012).
31. Huang, J. K. et al. High-κ perovskite membranes as insulators for two-dimensional transistors. *Nature* **605**, 262–267 (2022).
32. Hong, C. et al. Anomalous intense coherent secondary photoemission from a perovskite oxide. *Nature* **617**, 493–498 (2023).
33. Fujiwara, K. et al. Insulator-to-Metal Transition of Cr₂O₃ Thin Films via Isovalent Ru³⁺ Substitution. *Chem. Mater.* **32**, 5272–5279 (2020).
34. Matsumoto, T. et al. Experimental data collection and data access software through internet at SPring-8. *AIP Conf. Proc.* **2054**, 060076 (2019).
35. Nagaosa, N., Sinova, J., Onoda, S., MacDonald, A. H. & Ong, N. P. Anomalous Hall effect. *Rev. Mod. Phys.* **82**, 1539–1592 (2010).
36. Bousquet, E. & Cano, A. Non-collinear magnetism in multiferroic perovskites. *J. Phys. Condens. Matter* **28**, 123001 (2016).
37. Bertaut, E. F. *Magnetism*, Vol. 3. (New York: Academic, 1963).
38. Palacios, E., Bartolome, J., Luis, F. & Sonntag, R. Nuclear polarization of Nd in the pseudocubic perovskite NdAlO₃ studied by neutron diffraction below 1 K. *Phys. Rev. B Condens. Matter Mater. Phys.* **68**, 224425 (2003).

39. Plaza, I. et al. Neutron diffraction study of NdScO$_3$ below 1 K Magnetic structure and hyperfine enhanced polarization of Nd. *Phys. B Condens. Matter* **234–236**, 635–636 (1997).

40. Plaza, I. et al. Neutron diffraction study of the magnetic ordered Nd^{3+} in NdCoO$_3$ and NdInO$_3$ below 1 K. *Phys. B Condens. Matter* **234–236**, 632–634 (1997).

41. Tokunaga, Y. et al. Composite domain walls in a multiferroic perovskite ferrite. *Nat. Mater.* **8**, 558–562 (2009).

42. Evans, P. G., Chen, Y., Tilka, J. A., Babcock, S. E. & Kuech, T. F. Crystallization of amorphous complex oxides: New geometries and new compositions via solid phase epitaxy. *Curr. Opin. Solid State Mater. Sci.* **22**, 229–242 (2018).

43. Momma, K. & Izumi, F. Vesta 3 for three-dimensional visualization of crystal, volumetric and morphology data. *J. Appl. Crystallogr.* **44**, 1272–1276 (2011).

44. Zhou, H. D. & Goodenough, J. B. Localized or itinerant TiO$_3$ electrons in RTiO$_3$ perovskites. *J. Phys. Condens. Matter* **17**, 7395–7406 (2005).

45. Liu, B. et al. Electrical transport properties of La$_{1-x}$Sr$_x$CoO$_3$ thin films. *J. Appl. Phys.* **120**, 154103 (2016).

46. Dabrowski, B. et al. Structural, transport, and magnetic properties of RMnO$_3$ perovskites (R = La, Pr, Nd, Sm, Eu, Dy). *J. Solid State Chem.* **178**, 629–637 (2005).

47. Niwa, E. et al. Dependence of crystal symmetry, electrical conduction property and electronic structure of LnFeO$_3$ (Ln: La, Pr, Nd, Sm) on kinds of Ln^{3+}. *J. Ceram. Soc. Japan* **123**, 501–506 (2015).

48. Subramanian, M. A., Aravamudan, G. & Subba Rao, G. V. Oxide pyrochlores - A review. *Prog. Solid State Chem.* **15**, 55–143 (1983).

49. Sakai, T., Adachi, G., Shiokawa, J. & Shin-ike, T. Electrical conductivity of LnVO$_3$ compounds. *Mater. Res. Bull.* **11**, 1295–1299 (1976).

50. Hallas, A. M. et al. Coexistence of metallic and nonmetallic properties in the pyrochlore Lu$_2$Rh$_2$O$_7$. *npj Quantum Mater.* **4**, 9 (2019).

Acknowledgements

Author contributions

Conceptualization: L.F.Z., T.C.F. Methodology: MinoruK, H.K., M.T. Investigation: L.F.Z., T.C.F., Y.M., MinoruK, H.K., M.T. Visualization: L.F.Z. Supervision: T.C.F., M.K. Writing—original draft: L.F.Z., T.C.F. Writing—review & editing: T.C.F., MinoruK, T.A., H.K., M.T., M.K.

Competing interests

The authors declare no competing interests.

Additional information

Supplementary information The online version contains supplementary material available at https://doi.org/10.1038/s43246-024-00470-y.

Correspondence and requests for materials should be addressed to Takahiro C. Fujita.

Peer review information *Communications Materials* thanks Felix Gunkel and the other, anonymous, reviewers for their contribution to the peer review of this work. A peer review file is available.

Reprints and permissions information is available at http://www.nature.com/reprints

Publisher's note Springer Nature remains neutral with regard to jurisdictional claims in published maps and institutional affiliations.